RSC Advances

PAPER

View Article Online
View Journal | View Issue

Cite this: *RSC Adv.*, 2026, **16**, 20295

Sn-MOF/Zn-MOF composite electrode with interfacial synergy for high-performance battery-supercapacitor hybrid devices

Asmaa Fathy Abd Elaziz Kassem,[a] Ebraheem Abdu Musad Saleh,[a] K. Mahmud,[b] Muhammad Zahir Iqbal, *[bc] Abhinav Kumar, [de] Ismail Hassan,[a] Marwa Mostafa Moharam Haqqi Mohammed,[a] Kakul Husain,[a] Nusiba Mohammed Modawe Alshik[a] and Walaa Ibrahim Ahmed Ibrahim[fg]

The growing demand for reliable and high-performance energy storage devices obliges the development of novel materials that can merge high energy density with rapid charge–discharge capability. Hybrid supercapacitors offer this balance, while MOFs are recognized as promising electrode candidates due to their high surface area and tuneable structure. In this study, a Zn-MOF/Sn-MOF composite framework was synthesized and characterized thoroughly. Electrochemical analysis using CV, GCD, and EIS in both three- and two-electrode assemblies demonstrated that the composite exhibits significantly better performance than the individual pristine MOFs. The Zn-MOF/Sn-MOF//AC device exhibited a specific capacity of 356 C g^{-1} at 0.6 A g^{-1}. Correspondingly, the maximum energy and power densities of 79.2 Wh kg^{-1} and 4000 W kg^{-1}, respectively, were achieved. Moreover, the semi-empirical modelling navigation provided insights into the charge storage mechanism, confirming a synergistic effect in the composite. These findings highlight the potential of Sn-MOF/Zn-MOF as a high-performance electrode material for bridging the gap between batteries and supercapacitors.

Received 7th February 2026
Accepted 30th March 2026

DOI: 10.1039/d6ra01103a

rsc.li/rsc-advances

Introduction

The advancements of the modern world have increased energy consumption and demand. Conventional energy resources such as natural gas, coal and oil are finite, and they also pose great environmental risks. The alarming levels of pollution index and global warming indicate that these energy resources are unsustainable for long-term use.[1–3] The focus of today's world has shifted towards alternative renewable energy options such as hydropower, solar or wind energies. These alternatives are not only abundant but also clean and environmentally friendly.[4–6] However, their output fluctuates as they are much dependent on the time of the day and weather. To maintain the parity between supply and demand, the development of a balanced and efficient energy storage system is inevitable.[7,8] Electrochemical energy storage devices (EESDs) such as rechargeable batteries (RBs) and electrochemical supercapacitors (ESCs) are the most established systems that could facilitate the transition from conventional to more efficient non-conventional resources.[9–12] The non-faradaic electrostatic energy storage mechanism of ESCs enables exceptionally rapid charge–discharge cycles, high power density and remarkable cyclic stability.[13,14]

In contrast, RBs offer high energy density but with a shorter life and slower kinetics. Therefore, an efficient energy storage system is required that offers both high energy and high power densities.[15,16] Among ESCs and RBs, neither technology meets the increasing need for devices that show both properties simultaneously. Hybrid supercapacitors bridge the gaps between these two systems by integrating capacitor-type non-faradaic electrodes with faradaic battery-type electrodes.[17,18] These hybrid systems offer both high energy density without compromising power density and cyclic stability.[18–20] Their performance such as durability, ionic mobility and charge storage capacity mainly depend on the choice of electrode material. For the fabrication of HSCs, different materials have been investigated including phosphates, sulphides, transition-metal oxides and conducting polymers.

In recent decades, metal–organic frameworks (MOFs) have received notable attention because of their well-defined

[a]*Department of Chemistry, College of Science and Humanities in Al-Kharj, Prince Sattam Bin Abdulaziz University, Al-Kharj 11942, Saudi Arabia*
[b]*Unal Center of Education, Research and Development (UCERD), Rawalpindi, 44000, Pakistan. E-mail: nanotechenergy5@gmail.com*
[c]*University of the Punjab, Quaid-e-Azam Campus, Lahore 54590, Pakistan*
[d]*Department of Technical Sciences, Western Caspian University, Baku, Azerbaijan*
[e]*Centre for Research Impact & Outcome, Chitkara University Institute of Engineering and Technology, Chitkara University, Rajpura, 140401, Punjab, India*
[f]*Department of Chemistry, College of Science, University of Ha'il, Ha'il 81451, Saudi Arabia*
[g]*Medical and Diagnostic Research Center, University of Ha'il, Ha'il 55473, Saudi Arabia*

crystalline networks, large surface areas and tuneable pore structures. Derived from the coordination bonding between metals and organic molecules, MOFs offer continuous electrolyte diffusion channels and abundant active sites.[21–23] These characteristics make them highly suitable for applications such as environmental remediation and energy storage applications.[24–27] However, metal alloys are being used as self-supporting porous electrodes.[28] Untreated pristine MOFs have limited mechanical strength and poor electrical conductivity.[29–31] Hence, MOFs are often interlinked with polymers or conductive carbon supports to form composite structures, thereby overcoming these limitations through synergistic effects.[9,32] Sn-MOFs offer rich redox activity and high charge storage due to their multiple oxidation states.[33] Zn-based MOFs typically offer high surface areas and accessible porosity for rapid ion diffusion.[34] Hence, combining the rich redox activity of Sn-MOFs with the high surface area and fast ion-transport pathways of Zn-MOFs can enable more efficient charge storage can be realized.

Recently, MOF–MOF composite architectures have attracted considerable attention as the incorporation of two distinct MOFs can combine the benefits of their complementary pore structures, redox-active sites, and metal centers within a single framework.[35] Such rational combinations can enhance charge transport, ion diffusion, and electrochemical activity, making these composites highly promising for advanced energy storage devices.[36–38] Moreover, MOF–MOF composite structures can exhibit long-term stability compared to their individual parent MOFs.[37] Such composites could enable efficient, stepwise charge transfer through synergistic interactions, resulting in enhanced charge transport and overall performance.[39] In hybrid supercapacitors, rationally engineered MOF–MOF composites could offer improved electrolyte interaction and structural durability during prolonged cycling, which highlight their potential integration in high-performance energy storage applications.[40]

In this work, Sn-MOF/Zn-MOF were synthesized through a solvothermal method, and its structural and morphological characterizations were conducted through XRD and SEM, which offered insights into their crystallinity and grain size distribution, respectively. The electrochemical characteristics of the MOF/MOF composite were examined using cyclic voltammetry (CV), galvanostatic charge discharge (GCD) and electrochemical impedance spectroscopy (EIS) analyses. Furthermore, the capacitive- and diffusive-controlled contributions of the hybrid device were evaluated through linear and quadratic model fittings.

Material synthesis and electrode preparation

Zinc nitrate hexahydrate ($Zn(NO_3)_2 \cdot 6H_2O$), tin chloride dihydrate ($SnCl_2 \cdot 2H_2O$), benzene tetracarboxylic acid (BTCA), dimethylformamide (DMF), and deionized water (DI) were used in the solvothermal synthesis of Sn-MOF and Zn-MOF. To synthesize Sn-MOF, a tin chloride solution (0.6 M) was prepared in DI water and BTCA (0.3 M) was dissolved in a DMF solution. Both solutions were then mixed to achieve a homogeneous mixture. The prepared solutions were poured into a Teflon-lined container and sealed properly. This was heated up to 140 °C for 18 h, and the obtained material was centrifuged to collect the desired product, which was dried later. In a similar way, Zn-MOF was prepared by dissolving zinc chloride (0.6 M) in DI water and BTCA (0.3 M) in a DMF solution. Both these solutions were subsequently mixed. The resulting mixture was transferred to a Teflon-lined vessel and tightly sealed. It was heated at 140 °C for 18 h, and the resulting product was collected by centrifugation, washed thoroughly with ethanol and DI water, and dried in an oven. For electrode fabrication, a slurry was prepared by mixing 80% active material, 10% acetylene black, and 10% polyvinylidene fluoride (PVDF) binder, with PVDF first dissolved in *N*-methyl-2-pyrrolidone (*N*MP). The slurry was mixed overnight using a stirrer to attain a homogeneous mixture. The prepared mixture was deposited on a nickel foam (current collector) and dried for 6 h at 75 °C in an oven. A schematic of the preparation of Sn-MOF, Zn-MOF and Sn-MOF/Zn-MOF is illustrated in Fig. 1.

Results and discussion

The crystallinity of the synthesized MOFs was determined through the powder XRD technique. The XRD graph for both MOFs is displayed in Fig. 1(b), in which Zn-MOF shows well-defined and intense peaks. The main diffraction peaks are indexed to the crystallographic planes of (111), (201), (211), (112), (202), (013), (212), (113), (121), (022), (123), (222), (105), (131), and (224), in agreement with the JCPDS card 96-220-2688. Sn-MOF has broad peaks corresponding to the planes of (004), (203), (006), and (311), consistent with the JCPS card 96-221-9867. Debye–Scherrer calculations were employed to estimate the crystallite size from the XRD data, revealing average crystallite sizes of 4.01 nm for the Sn-MOF and 13.81 nm for Zn-MOF. The surface morphology was examined by scanning electron microscopy, revealing that Sn-MOF exhibited a granular morphology, whereas Zn-MOF presented crystalline structures distributed over the surface, as shown in Fig. 1(c and d). The electrochemical measurements (CV, GCD, and EIS) were performed using a potentiostat in a half-cell assembly, where platinum and Hg/HgO were used as the counter and reference electrodes, respectively. The best-performing electrode (Sn-MOF/Zn-MOF) was further investigated in a two-electrode assembly. 1 M KOH aqueous electrolyte was employed in the subsequent electrochemical testing. Cyclic voltammetry (CV) was conducted to evaluate the charge storage behaviour and redox activity of the electrode materials. Fig. 2 summarises the CV profiles of Sn-MOF, Zn-MOF and the Sn-MOF/Zn-MOF composite. Fig. 2(a) shows the plot of current as a function of voltage for Sn-MOF at various scan rates (3 mV s^{-1} to 50 mV s^{-1}). Similarly, the CV profiles of Zn-MOF were recorded at same scan rates, as shown in Fig. 2(b). The existence of distinct redox peaks in both Sn-MOF and Zn-MOF indicated that charge storage was primarily governed by faradaic redox reactions. The CV profile of the Sn-MOF/Zn-MOF composite is displayed in Fig. 2(c). The attained peaks were relatively broader than those of the pristine materials. It suggested the synergistic interaction

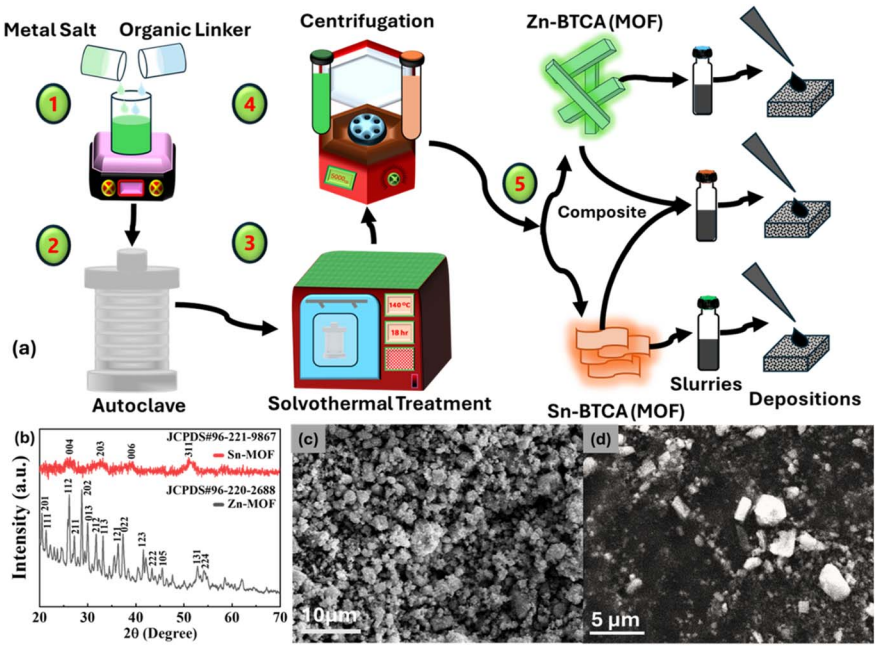

Fig. 1 (a) Schematic of the synthesis route for Sn-MOF and Zn-MOF. (b) X-ray diffraction patterns confirming the crystalline structures of Sn-MOF and Zn-MOF. (c–d) Surface morphology images of Sn-MOF and Zn-MOF.

of the two metal centres, paving the way towards faster charge kinetics and enhanced ion-diffusion pathways. With varying the scan rates, the characteristic peak shape remained intact. However, the peak positions were shifted slightly, which might be due to internal polarization. At higher scan rates, the composite material retained its CV profile. A comparison of the CV profiles at 3 mV s^{-1} is shown in Fig. 2(d). For the evaluation of the charge storage behaviour, galvanostatic charge–discharge (GCD) measurements were carried out. Fig. 3(a and b) show the GCD curves for Sn-MOF and Zn-MOF at various current densities. The GCD curves for the Sn-MOF/Zn-MOF composite material are shown in Fig. 3(c). A comparison of the GCD curves

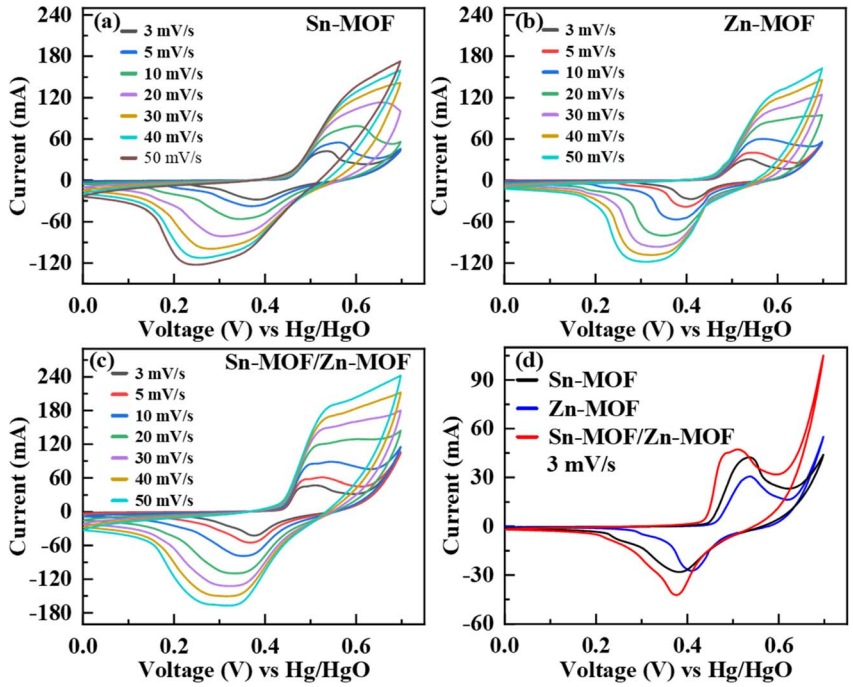

Fig. 2 Cyclic voltammetry curves of (a) Sn-MOF, (b) Zn-MOF, and (c) Sn-MOF/Zn-MOF composite. (d) Comparative CV curves of all samples recorded at a scan rate of 3 mV s^{-1}.

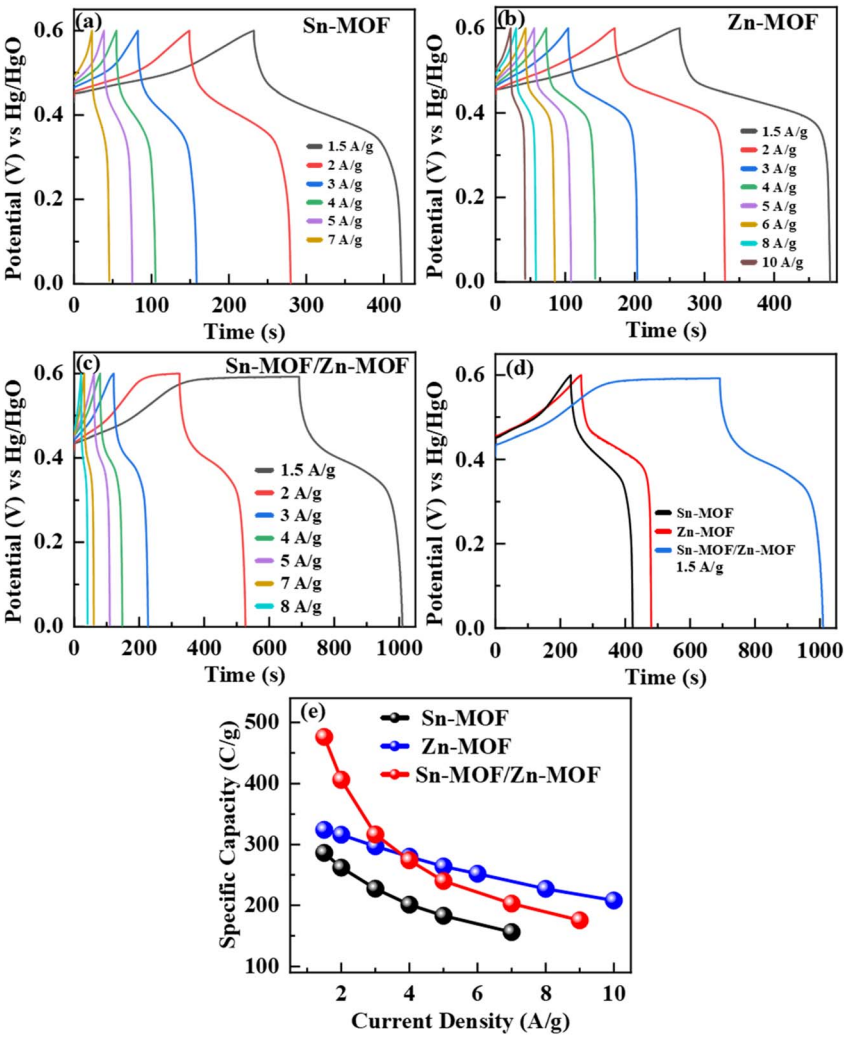

Fig. 3 Galvanostatic charge–discharge (GCD) profiles of (a) Sn-MOF, (b) Zn-MOF, and the (c) Sn-MOF/Zn-MOF composite. (d) Comparison of the GCD curves for all samples measured at a current density of 1.5 A g^{-1}. (e) Comparison of their specific capacities.

was carried out at 1.5 A g^{-1} for Sn-MOF, Zn-MOF and Sn-MOF/Zn-MOF. A clear difference could be observed for all three electrodes. Sn-MOF showed a moderate charge–discharge duration with a slightly sloped plateau, indicating its limited charge storage capability. In comparison, Zn-MOF delivered a longer charge–discharge time than Sn-MOF, demonstrating that it has a more efficient redox activity and higher capacity. The Sn-MOF/Zn-MOF composite electrode exhibited an extended discharge time, confirming its improved efficiency and superior charge storage performance at 1.5 A g^{-1}, as shown in Fig. 3(d). The trends in specific capacity at different current densities for all three electrodes (Sn-MOF, Zn-MOF and the Sn-MOF/Zn-MOF composite) are recorded in Fig. 3(e). The specific capacity of individual pristine MOFs was evaluated; it was 286 C g^{-1} for Sn-MOF and 324 C g^{-1} for Zn-MOF. However, the Sn-MOF/Zn-MOF composite delivered an improved specific capacity of 476 C g^{-1} at 1.5 A g^{-1}, highlighting its improved performance. It further demonstrated the effective utilization of active sites arising from the synergistic interaction between the two metal centres and improved electron transport. Specific capacity was calculated using the following equation.

$$Q_s = \left(\frac{I}{m}\right)\Delta t, \quad (1)$$

where Q_s indicates the specific capacity, I refer to the current, m is the mass, and Δt indicates the discharge time. Electrochemical impedance spectroscopy (EIS) was conducted over a frequency range of 0.01 Hz to 100 kHz to determine the resistive and diffusive contributions within the electrode system. Fig. 4(a–c) show the Bode plots, which depict impedance as a function of frequency for Sn-MOF, Zn-MOF and the Sn-MOF/Zn-MOF composite, respectively. Fig. 4(d) presents the Nyquist plots for pristine MOFs and the composite electrode, exhibiting the difference in their electrochemical behaviour. Zn-MOF presented an ESR value of 0.26 Ω, while Sn-MOF presented a slightly higher ESR of 0.45 Ω. The Sn-MOF/Zn-MOF composite exhibited an ESR of 0.31 Ω, which was an intermediate value between the two pristine MOFs. This suggested that the composite might partially inherit the favourable conductivity of

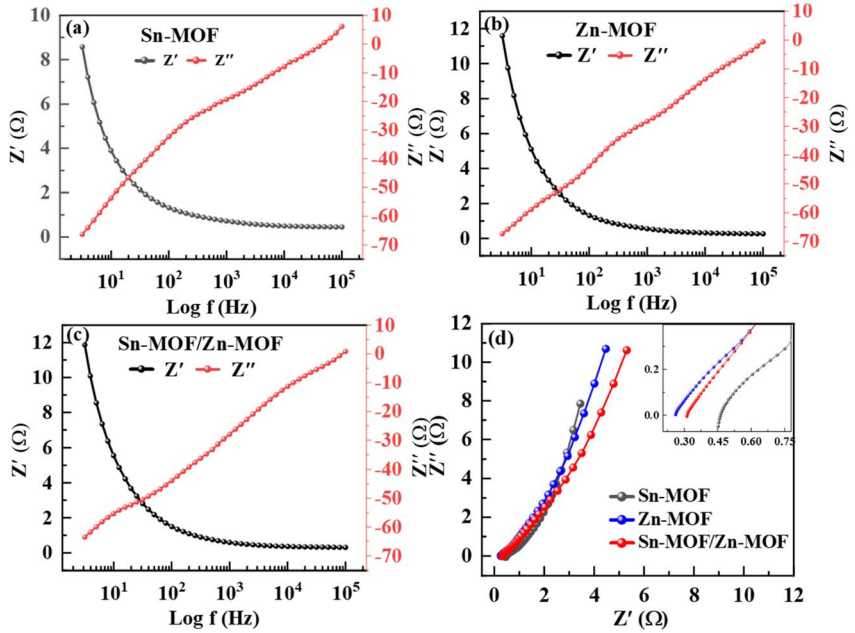

Fig. 4 Electrochemical impedance spectroscopy (EIS) results showing Bode plots of (a) Sn-MOF, (b) Zn-MOF, and (c) Sn-MOF/Zn-MOF composite, and (d) Nyquist plots of all these samples.

Zn-MOF while benefitting from the structural features introduced by Sn-MOF. This optimized resistance balance facilitates improved electrochemical performance by promoting efficient ion diffusion and enhanced redox activity.

A two-electrode configuration was employed to evaluate the performance of a real device. The Sn-MOF/Zn-MOF composite was used as the positive electrode, while the activated carbon (AC) served as the negative electrode, as shown in Fig. 5(a). The electrochemical performance of the device was tested in a 1 M KOH electrolyte solution. Fig. 5(b) presents the comparative CV behavior of the capacitive activated carbon electrode and the battery-type composite electrode at a scan rate of 10 mV s^{-1}. The hybrid device Sn-MOF/Zn-MOF//AC was further evaluated at different scan rates (3 mV s^{-1} to 100 mV s^{-1}) to determine its overall CV profile, as shown in Fig. 5(c). The prepared composite material retained its characteristics CV peak shape at higher scan rates. To examine the energy capability and charge storage properties of the device, the GCD profile of the assembled device at different current densities (0.6 A g^{-1} to 5 A g^{-1}) was evaluated, as shown in Fig. 6(a). The trend of the specific capacity as a function of current density is presented in Fig. 6(b) to evaluate the device performance. The lower current density provides adequate time for ion diffusion into the electrode, enabling full involvement in redox processes and yielding a maximum specific capacity of 356 C g^{-1} at 0.6 A g^{-1}. The energy and power densities of the device are presented in Fig. 6(c). The maximum value of energy density was 79.2 Wh kg^{-1} and that of power density was 4000 W kg^{-1}. The energy and power densities were calculated using the following equations.

$$E_s = \frac{Q_s \times \Delta V}{2 \times 3.6} \quad (2)$$

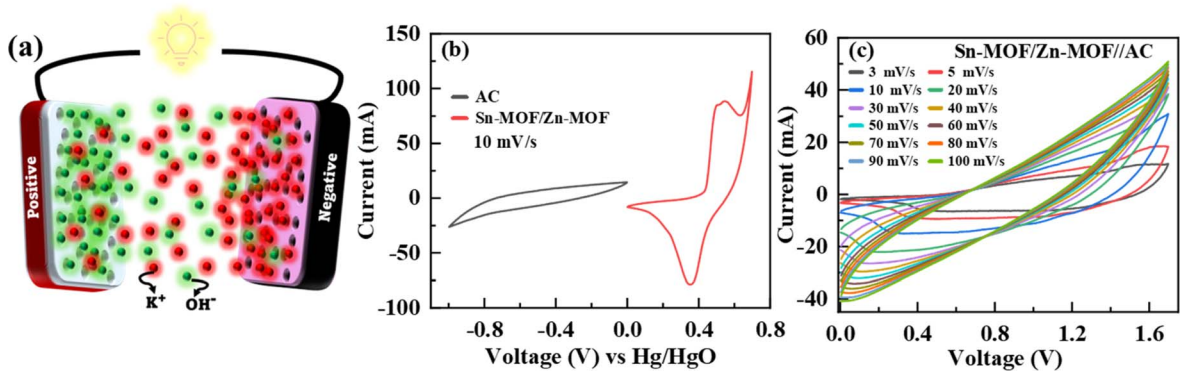

Fig. 5 (a) Schematic of the fabricated device. (b) CV comparison of the AC and Sn-MOF/Zn-MOF electrodes. (c) CV response of the assembled device.

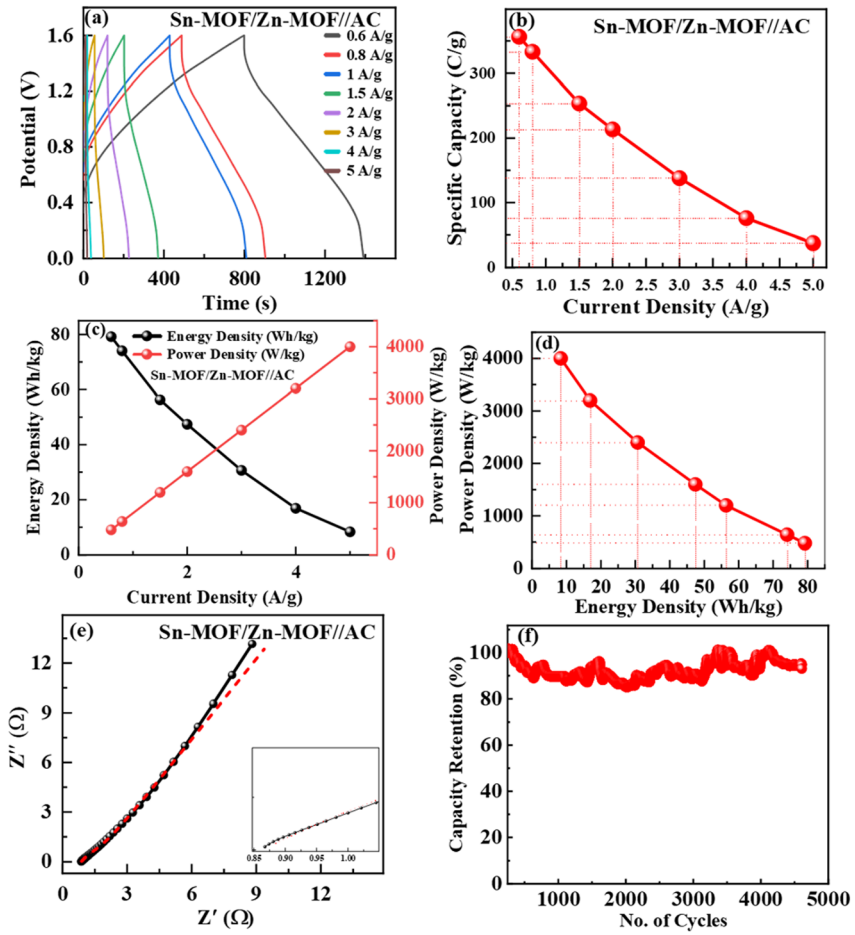

Fig. 6 Electrochemical evaluation of the assembled device: (a) GCD profile at different current densities. (b) Specific capacity *vs.* current density plot. (c) Energy and power densities as a function of current density. (d) Ragone plot (power density *vs.* energy density). (e) Nyquist plot with zoomed real impedance intercept. (f) Cyclic stability of the fabricated device.

$$P_s = \frac{E_s \times 3600}{\Delta t} \quad (3)$$

Here, E_s represent the specific energy density, Q_s is the specific capacity, ΔV is the potential window in which the device is tested, P_s is the specific power density, and Δt is the discharge time. Fig. 6(d) illustrates the Ragone plot, showing the relationship between the energy density and power density of the hybrid device. The Nyquist plot of the assembled device shows the typical features associated with the efficient energy transfer observed at higher frequency regions. A small real-axis intercept indicates low ESR and good electrode–electrolyte–collector interaction. The low-frequency inclined line reflects ion diffusion through the porous network. The steepness of this line indicated the presence of well-developed diffusion pathways and enhanced ion mobility inside the device architecture. The Nyquist profiles suggest that the assembled device exhibits low resistance, contributing efficiently to its strong electrochemical performance, as presented in Fig. 6(e). Fig. 6(f) depicts the cycling stability performance of the hybrid device, indicating the capacity retention after continuous electrochemical cycling. The capacitive and diffusive contributions of the hybrid device were estimated by fitting the linear model and quadratic model using the CV profile at the scan rates of 10 mV s^{-1}, 40 mV s^{-1}, and 100 mV s^{-1}, as shown in Fig. 7(a–c), respectively. The electrodes reflected a dominant diffusion-controlled contribution at lower scan rates because of the availability of ample time to access the deep active sites within the material. The diffusive contribution decreased with increasing scan rate while at higher scan rates, the capacitive contribution dominated due to limited time for ion diffusion into the material. This trend highlighted the electrode's fast response capability and indicated that the composite structure effectively supported both diffusion-driven and surface-controlled charge storage depending upon the operating conditions. The quadratic model reliably describes the current response across provided scan rates by capturing both the linear and non-linear components associated with redox behaviour and ion transport within the electrode. The strong agreement between the experimental curves and fitting profile offered by the quadratic model confirmed the suitability of the model in describing the electrode kinetics well at different scan rates. Fig. 7(d) illustrates a bar chart showing the percentage contributions of capacitive and diffusive-controlled processes obtained using the linear

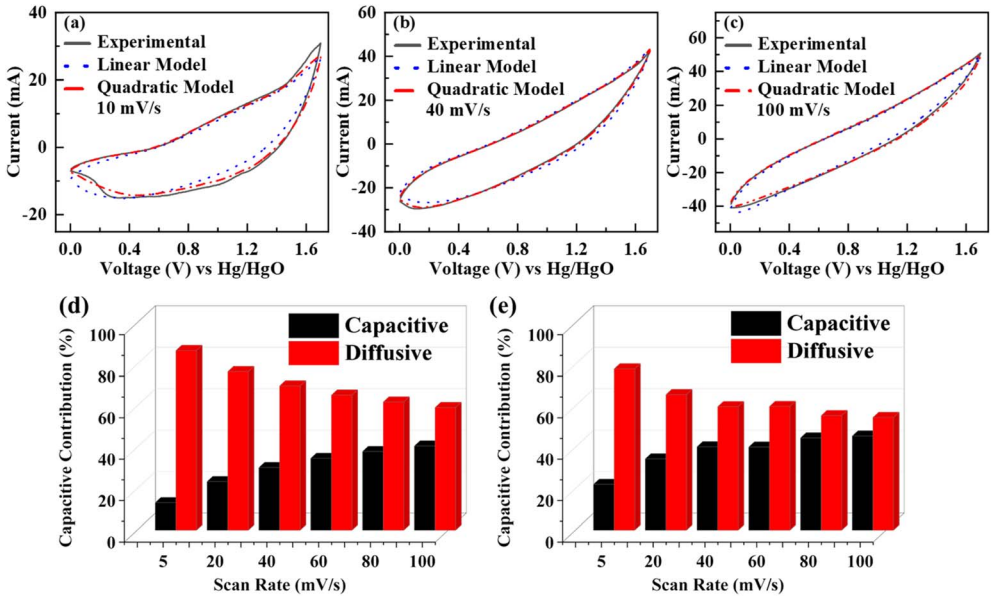

Fig. 7 (a–c) CV analysis of the device using linear and quadratic fitting. (d) Capacitive and diffusive contributions obtained from the linear model. (e) Capacitive and diffusive contributions obtained from the quadratic model.

model. The capacitive contribution increases with scan rate, while the diffusion-controlled contribution becomes more dominant at lower scan rates. At a lower scan rate, the attained capacitive and diffusive contributions were 13% and 87%, respectively. Similarly, at the highest scan rate, the obtained capacitive and diffusive contributions were found to be 40% and 60%, respectively. Fig. 7(e) illustrates a bar chart showing the percentage contributions of capacitive and diffusive-controlled processes obtained by employing the quadratic model. The diffusive contribution can be observed to reduce with increasing scan rates, which indicated that the electrodes stored charges through quick surface reactions as ions might not have gotten enough time to diffuse efficiently. On the other hand, capacitive contributions increased with increasing scan rates, which indicated the transition in the charge storage mechanism. The overall performance of the device governed by the combined action of capacitive- and diffusion-controlled processes clearly indicated the simultaneous involvement of both faradaic and non-faradaic reactions.

Conclusion

In this study, Sn-MOF, Zn-MOF and an Sn-MOF/Zn-MOF composite material were successfully synthesised and characterized. A systematic analysis was performed employing XRD, SEM and electrochemical evaluations. Both three electrodes and two electrodes configurations were employed to access electrochemical behavior using CV, GCD, and EIS techniques. In the half-cell assembly, the composite material exhibited the highest specific capacity of 476 C g^{-1} at 1.5 A g^{-1}, highlighting the mutual effect produced by the MOF/MOF combination. Based on this promising performance, the composite material was employed in a hybrid device assembly (Sn-MOF/Zn-MOF// AC), which demonstrated a maximum energy density of 79.2 Wh kg^{-1} and a power density of 4000 W kg^{-1}. Semi-empirical modelling approaches further supported the experimental findings to provide a deep insight into the charge storage mechanism. Overall, the interfacial synergy of Sn-MOF/Zn-MOF makes it a highly promising electrode material candidate for advanced energy storage applications, offering a balance between supercapacitor and battery performances.

Conflicts of interest

There are no conflict of interest to declare.

Data availability

This article contains no supplementary data. All data relevant to this study are included within the manuscript.

Acknowledgements

The authors extend their appreciation to Prince Sattam bin Abdulaziz University for funding this research work through the project number (PSAU/2025/01/34275).

References

1 K. Chandra Bhowmik, *et al.*, From lithium-ion to sodium-ion batteries for sustainable energy storage: a comprehensive review on recent research advancements and perspectives, *Chem. Rec.*, 2024, **24**(12), e202400176.
2 M. Hepel, Advances in micro-supercapacitors (MSCs) with high energy density and fast charge-discharge capabilities for flexible bioelectronic devices—a review, *Electrochem. Sci. Adv.*, 2023, **3**(3), e2100222.

3 N. Parvin, *et al.*, Recent advances in hybrid supercapacitors: a review of high performance materials and scalable fabrication techniques, *J. Mater. Chem. A*, 2025, 13.
4 L. S. Paraschiv and S. Paraschiv, Contribution of renewable energy (hydro, wind, solar and biomass) to decarbonization and transformation of the electricity generation sector for sustainable development, *Energy Rep.*, 2023, **9**, 535–544.
5 H. M. Saleh and A. I. Hassan, The challenges of sustainable energy transition: A focus on renewable energy, *Appl. Chem. Eng.*, 2024, **7**(2), 2084.
6 S. Algarni, *et al.*, Contribution of renewable energy sources to the environmental impacts and economic benefits for sustainable development, *Sustain. Energy Technol. Assessments*, 2023, **56**, 103098.
7 M. M. Islam, *et al.*, Improving reliability and stability of the power systems: a comprehensive review on the role of energy storage systems to enhance flexibility, *IEEE Access*, 2024, **12**, 152738–152765.
8 S. Sahoo and P. Timmann, Energy storage technologies for modern power systems: a detailed analysis of functionalities, potentials, and impacts, *IEEE Access*, 2023, **11**, 49689–49729.
9 H. Kuang, *et al.*, Dynamic diels-alder reaction crosslinked metal-organic framework/poly (ionic liquid) composite solid electrolyte for lithium-metal batteries, *J. Colloid Interface Sci.*, 2025, 139638.
10 G. Gupta, *et al.*, Intelligent regenerative braking control with novel friction coefficient estimation strategy for improving the performance characteristics of hybrid electric vehicle, *IEEE Access*, 2024, 12.
11 M. Jiang, *et al.*, Synergistic integration of internal gradient-doping and external coating for superior performance in lithium-rich Mn-based cathodes, *Chem. Eng. Sci.*, 2025, **314**, 121819.
12 T. Gao and Y. Wu, Applications and advances of machine learning in the development of solid-state electrolytes for lithium-ion batteries, *ACS Omega*, 2025, **10**(49), 60094–60109.
13 X. Chen, *et al.*, Advanced electrochromic energy storage devices based on conductive polymers, *Adv. Mater. Technol.*, 2024, **9**(21), 2301969.
14 A. Rajapriya, S. Keerthana, and N. Ponpandian, Fundamental understanding of charge storage mechanism, in *Smart Supercapacitors*, Elsevier, 2023, 65–82.
15 G. Smdani, *et al.*, Performance evaluation of advanced energy storage systems: a review, *Energy Environ.*, 2023, **34**(4), 1094–1141.
16 Z. Han, *et al.*, Dual regulation of anode corrosion and cathode oxygen evolution in alkaline sodium-ion batteries by hydrated eutectic electrolyte engineering, *Chem. Eng. J.*, 2026, 174384.
17 S. Rudra, *et al.*, Supercapatteries as hybrid electrochemical energy storage devices: current status and future prospects, *Molecules*, 2024, **29**(1), 243.
18 A. Patel, *et al.*, Review on recent advancements in the role of electrolytes and electrode materials on supercapacitor performances, *Discover Nano*, 2024, **19**(1), 188.
19 P. S. Kumar, *et al.*, A new highly powered supercapacitor electrode of advantageously united ferrous tungstate and functionalized multiwalled carbon nanotubes, *J. Power Sources*, 2021, **482**, 228892.
20 S. Ramar, *et al.*, Morphological tailoring of transition metal tungstate nanoreinforced composite: A key to unlock high-performance supercapacitors, *Energy Fuels*, 2025, **39**(21), 10070–10082.
21 J. Guo, *et al.*, Soft porous crystals: flexible MOFs as a new class of adaptive materials, *Ind. Chem. Mater.*, 2025, **3**(6), 651–680.
22 L. Yu, *et al.*, Nanoporous crystalline materials for the recognition and applications of nucleic acids, *Adv. Mater.*, 2025, **37**(31), 2305171.
23 Y. Qin, *et al.*, Hydrogen-bonded interfacial super-assembly of spherical carbon superstructures for high-performance zinc hybrid capacitors, *Nano-Micro Lett.*, 2026, **18**(1), 38.
24 Y. Nie, *et al.*, Metal organic framework coated MnO_2 nanosheets delivering doxorubicin and self-activated DNAzyme for chemo-gene combinatorial treatment of cancer, *Int. J. Pharm.*, 2020, **585**, 119513.
25 Y. Li, *et al.*, Efficient degradation of norfloxacin by synergistic activation of PMS with a three-dimensional electrocatalytic system based on Cu-MOF, *Sep. Purif. Technol.*, 2025, **356**, 129945.
26 Q. Zhou, *et al.*, Co_3S_4-pyrolysis lotus fiber flexible textile as a hybrid electrocatalyst for overall water splitting, *J. Energy Chem.*, 2024, **89**, 336–344.
27 Z. Li, *et al.*, Reliable strategy for the covalent bonding of MOFs to SiC membranes for ultrastable noble metal capture in harsh environments, *ACS Appl. Mater. Interfaces*, 2025, **17**(37), 52981–52992.
28 Y. Yu, *et al.*, Dealloying treated FeCoNiCuMo high-entropy alloy as a self-supporting porous electrode for overall water splitting, *J. Environ. Chem. Eng.*, 2025, **13**(3), 117127.
29 T. Wang, *et al.*, Approaches to enhancing electrical conductivity of pristine metal–organic frameworks for supercapacitor applications, *Small*, 2022, **18**(32), 2203307.
30 J. Ou, *et al.*, Pre-strain and release in MOF catalysts: Ligand-engineered strain storage for enhanced catalytic activity, *J. Colloid Interface Sci.*, 2025, 138325.
31 X. Yang, *et al.*, Enhancing electrochemical performance of CNTs-decorated K_3V_3 (PO4) 4@ C nanocomposite *via* Nd^{3+}-doping for advanced potassium energy storage, *Ceram. Int.*, 2025, 52.
32 M. S. Hossain, *et al.*, Polyaniline-functionalized jute fiber as a sustainable electrode for high-performance supercapacitors, *Mater. Adv.*, 2026, 7.
33 K. Liu, *et al.*, MOFs and their derivatives as Sn-based anode materials for lithium/sodium ion batteries, *J. Mater. Chem. A*, 2021, **9**(48), 27234–27251.
34 Q. Huang, *et al.*, A comprehensive review on zinc-based MOFs and their derivatives for alkali-ion batteries: synthesis, applications, and future prospects, *Adv. Funct. Mater.*, 2025, **35**(46), 2508749.
35 M. Lu, *et al.*, Core-shell MOF@ MOF composites for sensitive nonenzymatic glucose sensing in human serum, *Anal. Chim. Acta*, 2020, **1110**, 35–43.

36 B. Cui and G. Fu, Process of metal–organic framework (MOF)/covalent–organic framework (COF) hybrids-based derivatives and their applications on energy transfer and storage, *Nanoscale*, 2022, **14**(5), 1679–1699.
37 S. K. Gebremariam, *et al.*, MOF@ MOF core-shell hybrid adsorbents with controlled water vapor affinity towards enhanced and steady CO_2 capture in moist conditions, *Carbon Capture Sci. Technol.*, 2025, **14**, 100356.
38 H.-B. Huang, *et al.*, MOF@MOF hierarchical heterotructures for enhanced photocatalytic H_2O_2 production and furfuryl alcohol oxidation, *Chin. J. Struct. Chem.*, 2025, 100717.
39 Y. Chen, *et al.*, Multi-stepwise charge transfer *via* MOF@ MOF/TiO_2 dual-heterojunction photocatalysts towards hydrogen evolution, *J. Mater. Chem. A*, 2022, **10**(17), 9717–9725.
40 R. Bhosale, *et al.*, Recent progress on functional metal–organic frameworks for supercapacitive energy storage systems, *Energy Technol.*, 2023, **11**(9), 2300147.